New Journal of Physics
The open-access journal for physics

Quantum-beat analysis of the rotational–vibrational dynamics in D_2^+

M Winter[1], **R Schmidt**[2] **and U Thumm**[3,4]
[1] Max-Planck Institute for the Physics of Complex Systems, Nöthnitzer Str. 38,
D-01187 Dresden, Germany
[2] Institut für Theoretische Physik, Technische Universität Dresden,
D-01062 Dresden, Germany
[3] James R. Macdonald Laboratory, Kansas State University, Manhattan,
KS 66506-2604, USA
E-mail: thumm@phys.ksu.edu

New Journal of Physics **12** (2010) 023020 (20pp)
Received 20 October 2009
Published 16 February 2010
Online at http://www.njp.org/
doi:10.1088/1367-2630/12/2/023020

Abstract. The rapid ionization of D_2 in a short and intense laser pulse generates a rotational–vibrational (RV) nuclear wave packet in D_2^+. By solving the time-dependent Schrödinger equation in full dimensionality, we simulate the coherent evolution of such wave packets and discuss their ro-vibrational dynamics. Within a harmonic time-series analysis of the evolving nuclear probability density, we characterize the RV dynamics in D_2^+ in an external intense linearly polarized infrared laser field in terms of quantum-beat (QB) spectra in which both internuclear distance and molecular orientation relative to the linearly polarized laser field are resolved. Based on numerical examples for the nuclear dynamics without and under the influence of pulsed and continuum-wave (cw) laser light, we discuss and quantify the signature of RV couplings in QB spectra and the extent to which the QB analysis of measured time-dependent fragment kinetic energy release spectra is expected to image the laser-dressed RV structure of D_2^+.

---

[4] Author to whom any correspondence should be addressed.

Contents

1. Introduction

Within the past decade, intense ultrashort laser pulses with intensities in excess of $10^{15}\,\mathrm{W\,cm^{-2}}$ and durations of a few optical cycles have become available in many basic-research laboratories worldwide as valuable tools for time-resolved investigations of the bound and free (dissociating) motion of nuclei in excited molecules [1]–[14]. Such ultrashort laser pulses are being used in a rapidly increasing number of pump–probe experiments that destructively image the nuclear motion inside (small) molecules. In such experiments, a first short laser pulse, the pump pulse, has a bandwidth covering several rotational and vibrational excited molecular states, and generates a coherent ro-vibrational nuclear wave packet either in the neutral molecule or, following ionization, in the molecular ion. The time evolution of this nuclear wave packet is subsequently imaged with a second short, time-delayed, probe laser pulse. This second pulse quickly ionizes the excited molecule (or molecular ion), leading to its fragmentation by 'Coulomb explosion' (CE) [15, 16]. Rapid ionization (on the time scale of nuclear motion) by the probe pulse followed by the detection of the energy distribution of molecular fragments is the basic idea behind the CE-imaging technique that allows the reconstruction of nuclear dynamics: repeating these excitation (pump) and delayed CE (probe) steps for a sequence of pump–probe delay times τ provides a time series of kinetic energy release (KER) spectra [4]–[6], [17]–[19]. This sequence constitutes a 'molecular movie' that captures the temporal evolution of the nuclear probability density as a function of nuclear positions. Such 'movies' were shown experimentally to reveal, for example, the classical motion of nuclear wave packets' center of mass, as well as purely quantum mechanical effects, such as cycles of wave packet dephasing and revival [4, 6, 12, 17, 18, 20], in agreement with theoretical predictions [15].

Experiments that resolve in time the coherent nuclear motion are most conveniently performed and analyzed for diatomic molecules for which CE imaging can accurately map the distribution of internuclear distances R in the excited molecule (or molecular ion). This promotes our understanding of the evolution of a variety of molecular phenomena that are triggered by intense laser pulses, such as vibrational-state-resolved dissociation, ionization followed by fragmentation, the decoherence and dephasing of nuclear wave packets, and the transient formation of laser-induced bound molecular states ([10, 21, 22] and references therein). In particular, the most elementary molecules, H_2^+ and its isotopologues, are accessible to, and frequent targets of, experimental studies [4, 6, 7, 12], [17]–[19], and can be described in accurate calculations [16], [23]–[27]. While most experimental and theoretical investigations have studied molecular dynamics as a function of time and internuclear separation, recent experimental [10] and theoretical [21] investigations have found that much can be learned from a frequency analysis of the evolution of the excited nuclear wave function. As was shown previously in numerical simulations that neglect molecular rotation, Fourier analysis of a time series of spectral data over a finite interval of pump–probe delays $\tau \epsilon [0, T]$ yields R-dependent quantum-beat (QB) spectra that reveal the nodal structure of bound vibrational states of the lowest adiabatic potential curve of the molecular ion, together with the corresponding vibrational transition energies. This offers the prospect of imaging laser-dressed molecular potential curves [10, 21].

In the present work, we extend earlier investigations [10, 21, 28, 29] of laser-induced coherent nuclear dynamics in D_2^+ by adding molecular rotation [26, 27]. We significantly expand our previous exploratory work [27] on ro-vibrating D_2^+ molecules by presenting and discussing details of our calculation and spectral analysis, by considering a large range of QB frequencies, and by varying both laser intensity and pulse lengths from 10^{13} to 10^{14} W cm^{-2} and 25 fs to continuum wave (cw), respectively. The paper is structured as follows. In section 2.1, we describe our model for the interaction of one-electron diatomic molecular ions with an intense linearly polarized laser electric field. In section 2.2, we review our numerical method for solving the time-dependent Schrödinger equation (TDSE) which, in essence, combines the split-operator numerical propagation of adiabatic nuclear wave functions (with regard to R) and a basis-set expansion (with regard to the angle between the molecular axis and the laser electric field vector). Next, in section 2.3, we define QB spectra and discuss some of their general properties for the propagation of an initial ro-vibrational wave packet in a diatomic molecule without and under the influence of an external (pulsed or continuous) laser electric field. We conclude section 2 by modeling in section 2.4 the initial ro-vibrational nuclear wave packet in D_2^+ that results from the ionization of the neutral parent molecule (D_2) in an ultrashort intense pump laser pulse.

Numerical applications for the QB analysis of D_2^+ follow in section 3. The undistorted (free) evolution of the pump-laser-generated nuclear wave packet is examined in detail in section 3.1. However, instead of only following the evolution of the ro-vibrational probability density in time (see figure 1), we also study its frequency decomposition. This allows us to illustrate and distinguish rotational and vibrational effects and to quantify ro-vibrational couplings in QB spectra. Next, in section 3.2, we consider the ro-vibrational dynamics in D_2^+ in a 'probe pulse pedestal' in comparison with the field-free results of section 3.1. With such a pedestal, we attempt to model the influence a realistic probe pulse has on the nuclear evolution prior to destructively imaging the probability density of molecular ions. In section 3.3, we consider the interaction of the molecular ion with a cw laser field. Our analysis of the coupling of rotational and vibrational motion during the evolution of the nuclear wave packet in section 3 is facilitated by comparisons with both previous investigations [10, 21] that disregard molecular

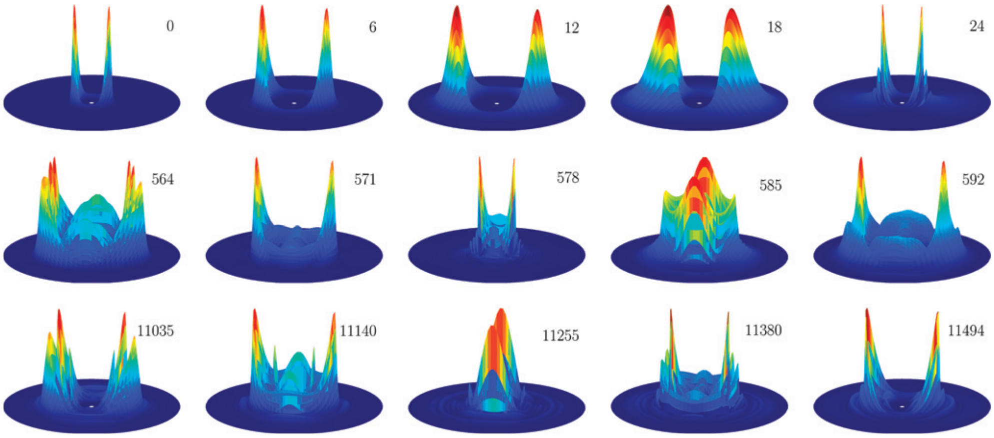

Figure 1. Snapshots of the nuclear-density evolution for the field-free propagation of a ro-vibrational nuclear wave packet in D_2^+. Top: first vibrational period at times 0, 6, 12, 18 and 24 fs. Middle: vibrational revival at times 564, 571, 578, 585 and 592 fs. Bottom: rotational revival at times 11 035, 11 140, 11 255, 11 380 and 11 494 fs.

rotations, and with the limiting cases of rigid rotors and aligned molecular ions. In section 3.5, we investigate the dependence of QB spectra for the ro-vibrating D_2^+ molecular ion on laser intensity and pulse length. Our conclusions are given in section 4.

We use atomic units throughout this work, unless otherwise indicated, and designate the vibrational ground states of D_2 and D_2^+ with the index $\nu = 0$ and excited states with $\nu \geqslant 1$.

2. Theory

2.1. Formal solution of the time-dependent Schrödinger equation

After separating the center-of-mass motion, the TDSE of the D_2^+ molecular ion in a laser field is given by

$$\mathrm{i}\frac{\partial}{\partial t}\psi(\vec{R},\vec{r},t) = \hat{H}\psi(\vec{R},\vec{r},t). \quad (1)$$

The vector $\vec{R}$ identifies the internuclear distance, $\vec{r}$ the electronic coordinate in the center-of-mass system (CMS), and the Hamiltonian can be written as

$$\begin{aligned} \hat{H} &= \hat{T} + \hat{H}_{\mathrm{el}}(\vec{r};\vec{R}) + \epsilon(t)z, \\ \hat{H}_{\mathrm{el}}(\vec{r};\vec{R}) &= \frac{\hat{\vec{p}}^{\,2}}{2} + \frac{1}{|\vec{R}|} - \frac{1}{|\vec{r}-\frac{1}{2}\vec{R}|} - \frac{1}{|\vec{r}+\frac{1}{2}\vec{R}|}, \end{aligned} \quad (2)$$

where the operator $\hat{\vec{T}}$ relates to the kinetic energy of the relative motion of the nuclei and $\hat{\vec{p}}$ to the momentum of the electron. The laser electric field

$$\epsilon(t) = \epsilon_0 f(t)\cos\omega_{\mathrm{L}}t \quad (3)$$

is assumed to be linearly polarized along the z-direction and is expressed in terms of the carrier frequency ω_{L}, the maximal field amplitude ϵ_0 and the envelope function $f(t)$.

We numerically solve the electronic Schrödinger equation,

$$\hat{H}_{\mathrm{el}}(\vec{r};\vec{R})\varphi_i(\vec{r};\vec{R}) = E_i(R)\varphi_i(\vec{r};\vec{R}), \tag{4}$$

separately for a large number of fixed internuclear distances, in order to obtain the adiabatic electronic wave functions $\{\varphi_i\}$ and the corresponding energy surfaces, $\{E_i(R)\}$. The expansion of the total wave function in (1) in terms of the complete set of electronic wave functions,

$$\psi(\vec{R},\vec{r},t) = \sum_i \Omega_i(\vec{R},t)\varphi_i(\vec{r};\vec{R}), \tag{5}$$

defines the nuclear wave functions $\{\Omega_i(\vec{R},t)\}$. Inserting this Born–Oppenheimer (BO) expansion into (1), followed by projection on to individual adiabatic electronic states, leads to a set of coupled differential equations for the nuclear wave functions. By neglecting the non-BO couplings,

$$\int \mathrm{d}^3 r \varphi_j^*(\vec{r};\vec{R})\vec{\nabla}_{\mathrm{R}}\varphi_i(\vec{r};\vec{R}) \tag{6}$$

and

$$\int \mathrm{d}^3 r \varphi_j^*(\vec{r};\vec{R})\Delta_{\mathrm{R}}\varphi_i(\vec{r};\vec{R}), \tag{7}$$

while retaining all couplings induced by the laser electric field (in dipole approximation for the electric field),

$$\epsilon(t)d_{ij}(\vec{R}) = \epsilon(t)\int \mathrm{d}^3 r \varphi_i^*(\vec{r};\vec{R}) z \varphi_j(\vec{r};\vec{R}), \tag{8}$$

the contact transformation

$$\Omega_i(R,\theta,t) = \frac{\Xi_i(R,\theta,t)}{R} \tag{9}$$

allows the set of differential equations for the components of the nuclear wave function

$$\vec{\Xi}(R,\theta,t) = (\Xi_1(R,\theta,t), \Xi_2(R,\theta,t), \ldots) \tag{10}$$

to be written as

$$\mathrm{i}\frac{\partial}{\partial t}\vec{\Xi}(R,\theta,t) = (\hat{T} + \hat{E}(R) + \hat{D}(R,\theta,t))\vec{\Xi}(R,\theta,t). \tag{11}$$

This equation includes the nuclear kinetic energy

$$\hat{T} = -\frac{1}{2\mu}\frac{\partial^2}{\partial R^2} + \frac{\hat{\vec{L}}^2}{2\mu R^2}, \tag{12}$$

with reduced mass μ, the nuclear angular momentum operator

$$\hat{\vec{L}}^2 = \frac{1}{R^2 \sin\theta}\frac{\partial}{\partial\theta}\sin\theta\frac{\partial}{\partial\theta} + \frac{1}{R^2\sin^2\theta}\frac{\partial^2}{\partial\varphi^2}, \tag{13}$$

and the matrix representations in the set of adiabatic electronic wave functions $\{\varphi_i\}$ of the energy operator $\hat{E}(R)$,

$$E_{ij}(R) = E_i(R)\delta_{ij}, \tag{14}$$

and the dipole transition operator $\hat{D}(R)$,

$$D_{ij}(R) = d_{ij}(R,\theta)\epsilon(t). \tag{15}$$

We truncate this system of infinitely many coupled differential equations, assuming that only the few lowest potential surfaces are populated and noticeably coupled by the interaction with the laser field. This results in a finite and numerically accessible system. In general, this neglect of non-BO couplings that would populate higher potential surfaces is justified since nuclear motion occurs on a much slower time scale than electronic motion. We note, however, that this approximation may break down near avoided crossings of two BO-potential surfaces where electronic wave functions change in character and depend more sensitively on nuclear coordinates.

By formulating the set of equations (11), we represented the nuclear wave functions in spherical coordinates. Due to cylindrical symmetry about the internuclear axis, the angular momentum P_φ (related to the last term in (13)) is conserved. Therefore, the nuclear molecular wave functions $\{\Xi_i(R,\theta,t)\}$ depend solely on φ, the angle designating the rotation of $\vec{R}$ about the laser electric field vector, through the factor $\mathrm{e}^{\mathrm{i}m\varphi}$.

2.2. *Numerical propagation of nuclear wave functions*

We calculated the adiabatic potential surfaces $E_i(R)$ in (4) and the corresponding dipole transition moments (8) using the code *dymol* [30] based on an expansion in atomic s, p and d orbitals centered at the two nuclei [31]. At each nucleus, we used 59 basis functions. The BO surfaces were calculated for internuclear distances from $R = 1$ to $R = 10$ with a step size of $\Delta R = 0.1$ and additional points at $R = 11, 12, \ldots, 15$. Comparing the calculated surfaces with [32], we found deviations of the order of 10^{-5}. As another test of our numerical accuracy, we investigated the behavior of adiabatic potential energy surfaces and dipole couplings at large internuclear distances. We verified that in this limit (i) our calculated surfaces are eigenstates of the H atom and (ii) the dipole moment induced by $\sigma_\mathrm{g} - \sigma_\mathrm{u}$ coupling becomes $R/2$, while (iii) the $\sigma_\mathrm{g} - \pi_\mathrm{u}$ dipole moment assumes the value of the atomic 1s–2p coupling.

We propagate the vector of nuclear wave function components $\vec{\Xi}(R,\theta,t)$ using the split operator method [29, 33] implemented in the code *WavePacket* [34] and approximate the time-evolution operator by a product of exponential operators:

$$\begin{aligned}\vec{\Xi}(R,\theta,t+\Delta t) &= \mathrm{e}^{-\mathrm{i}\int_t^{t+\Delta t}\mathrm{d}t'\hat{H}(t')}\vec{\Xi}(R,\theta,t)\\ &\approx \mathrm{e}^{-\mathrm{i}\hat{E}(R)\Delta t/2}\,\mathrm{e}^{-\mathrm{i}\hat{D}(R,\theta,t)\Delta t/2}\,\mathrm{e}^{-\mathrm{i}\hat{T}\Delta t}\,\mathrm{e}^{-\mathrm{i}\hat{D}(R,\theta,t)\Delta t/2}\,\mathrm{e}^{-\mathrm{i}\hat{E}(R)\Delta t/2}\vec{\Xi}(R,\theta,t)+\mathcal{O}(\Delta t^3).\end{aligned} \tag{16}$$

We choose Δt small enough so that $\hat{H}$ can be assumed to be time independent in the small time intervals $[t, t+\Delta t]$ and evaluate the Hamiltonian at the point t of each interval. For all numerical applications in this work, we included the three lowest potential surfaces $E_i(R), i = 1, \ldots, 3$

corresponding to the adiabatic electronic states φ_i, $i = 1, \ldots, 3$ with symmetries σ_g, σ_u and π_u, respectively. For more details on our numerical method, see appendices A and B.

2.3. Quantum-beat spectra

In this section, we describe our computation of ro-vibrational QB spectra based on the nuclear probability densities $\{|\Xi_i(R, \theta, t)|^2\}$. Following our definition of power spectra and spectral line strengths in section 2.3.1, we analyze these quantities for the special cases of field-free propagation (section 2.3.2) and propagation of ro-vibrational nuclear wave packets in cw laser fields (section 2.3.3).

2.3.1. Power spectra and line strengths. Due to the orthogonality of the electronic wave functions φ_i defined in (4), the nuclear probability density is the sum of the densities on each BO surface:

$$\varrho(R, \theta, t) = \sum_i |\Xi_i(R, \theta, t)|^2. \tag{17}$$

Subtracting the time-independent finite-time average

$$\bar{\varrho}(R, \theta) = \frac{1}{T} \int_0^T \mathrm{d}t\, \varrho(R, \theta, t) \tag{18}$$

from the density, we obtain

$$c(R, \theta, t) = \varrho(R, \theta, t) - \bar{\varrho}(R, \theta). \tag{19}$$

By subtracting $\bar{\varrho}$, all time-independent terms are removed. This is desirable, because (i) these static terms do not describe transitions between ro-vibrational states and (ii) they would lead to a huge background in the power spectra near frequencies $f = 0$. Fourier transformation over the finite sampling time T results in the complex-valued probability density

$$\tilde{c}(R, \theta, f) = \int_0^T \mathrm{d}t\, c(R, \theta, t)\, \mathrm{e}^{-\mathrm{i}2\pi f t}. \tag{20}$$

The density $\tilde{c}(R, \theta, f)$ leads to the following spectra, which constitute the main subject of our numerical applications below. While the fully differential power spectrum is given by $|\tilde{c}(R, \theta, f)|^2$, for illustrative purposes it is advantageous to define the R- and θ-dependent power spectra

$$A(R, f) = \left| \int \mathrm{d}\theta \sin(\theta) \tilde{c}(R, \theta, f) \right|^2 \tag{21}$$

and

$$W(\theta, f) = \left| \int \mathrm{d}R\, \tilde{c}(R, \theta, f) \right|^2, \tag{22}$$

respectively, and the corresponding spectral line intensities

$$\mathscr{A}(f) = \int \mathrm{d}R\, A(R, f) \tag{23}$$

and

$$\mathscr{W}(f) = \int \mathrm{d}\theta \sin(\theta) W(\theta, f). \tag{24}$$

2.3.2. Field-free propagation. Without laser interactions, the Hamiltonian (2) is time independent and allows the separation of temporal and spatial parts in the stationary nuclear wave functions of the D_2^+ molecular ion. Assuming that the ro-vibrational wave packet is initially on the BO ground-state surface $E_1(R)$, and because of our neglect of weak non-BO couplings mentioned earlier, we only need to consider the nuclear wave function $\Xi_1(R, \theta, t)$. We expand this wave packet in terms of stationary vibrational states $\chi_{\nu,l}(R)$ and rotational wave functions (Legendre polynomials) $P_l(\theta)$,

$$\Xi_1(R, \theta, t) = \sum_{\nu,l} a_{\nu l}\, \mathrm{e}^{-\mathrm{i}E_{\nu l}t} \chi_{\nu,l}(R) P_l(\theta), \tag{25}$$

where the ro-vibrational energies are designated as $E_{\nu l}$.

The vibrational and rotational wave functions satisfy the orthogonality relations

$$\int_0^{\pi} \mathrm{d}\theta \sin\theta\; P_l(\theta) P_{l'}(\theta) = \delta_{l,l'} \tag{26}$$

and

$$\int_0^{\infty} \mathrm{d}R\, \chi_{\nu l}(R) \chi^*_{\nu' l'}(R) = \begin{cases} \delta_{\nu,\nu'}, & \text{for } l = l', \\ S_{\nu l,\nu' l'}, & \text{for } l \neq l'. \end{cases} \tag{27}$$

Following the general procedure given in the previous subsection, we remove all diagonal terms ($\nu = \nu'$ and $l = l'$) by subtracting the time-independent finite-time average and obtain

$$\begin{aligned} c(R, \theta, t) &= \varrho(R, \theta, t) - \bar{\varrho}(R, \theta) \\ &= \sum_{\nu\neq\nu', l\neq l'} a_{\nu l} a^*_{\nu' l'} \chi_{\nu l}(R) P_l(\theta) \chi^*_{\nu' l'}(R) P_{l'}(\theta) \mathrm{e}^{-\mathrm{i}(E_{\nu l} - E_{\nu' l'})t} \\ &\quad + \sum_{\nu, l\neq l'} a_{\nu l} a^*_{\nu l'} \chi_{\nu l}(R) \chi^*_{\nu l'}(R) P_l(\theta) P_{l'}(\theta) \mathrm{e}^{-\mathrm{i}(E_{\nu l} - E_{\nu l'})t} \\ &\quad + \sum_{\nu\neq\nu', l} a_{\nu l} a^*_{\nu' l} \chi_{\nu l}(R) \chi^*_{\nu' l}(R) P_l^2(\theta) \mathrm{e}^{-\mathrm{i}(E_{\nu l} - E_{\nu' l})t}. \end{aligned} \tag{28}$$

Fourier transformation over the finite time interval $[0, T]$ yields the complex-valued function

$$\begin{aligned} \tilde{c}(R, \theta, f) &= \int_0^T \mathrm{d}t\, c(R, \theta, t)\, \mathrm{e}^{-\mathrm{i}2\pi f t} \\ &= \sum_{\nu\neq\nu', l\neq l'} a_{\nu l} a^*_{\nu' l'} \chi_{\nu l}(R) P_l(\theta) \chi^*_{\nu' l'}(R) P_{l'}(\theta) \delta_T(f_{\nu l,\nu' l'} - f) \\ &\quad + \sum_{\nu, l\neq l'} a_{\nu l} a^*_{\nu l'} \chi_{\nu l}(R) \chi^*_{\nu l'}(R) P_l(\theta) P_{l'}(\theta) \delta_T(f_{\nu l,\nu l'} - f) \\ &\quad + \sum_{\nu\neq\nu', l} a_{\nu l} a^*_{\nu' l} \chi_{\nu l}(R) \chi^*_{\nu' l}(R) P_l^2(\theta) \delta_T(f_{\nu l,\nu' l} - f), \end{aligned} \tag{29}$$

where $\delta_T(f) = \int_0^T \mathrm{d}t\, \mathrm{e}^{-\mathrm{i}2\pi f t}$ and $2\pi f_{\nu l,\nu' l'} = E_{\nu l} - E_{\nu' l'}$.

Integrating $|\tilde{c}(R,\theta,f)|^2$ over either θ or R, while taking advantage of orthogonality relations (26) and (27), we obtain the R- and θ-dependent power spectra

$$A(R,f)=\left|\sum_{v\neq v',l} a_{vl}a^*_{v'l}\chi_{vl}(R)\chi^*_{v'l}(R)\delta_T(f_{vl,v'l}-f)\right|^2 \tag{30}$$

and

$$W(\theta,f)=\left|\sum_{v,l\neq l'} a_{vl}a^*_{vl'}S_{vl,vl'}P_l(\theta)P_{l'}(\theta)\delta_T(f_{vl,vl'}-f)\right.$$
$$\left.+\sum_{v\neq v',l\neq l'} a_{vl}a^*_{v'l'}S_{vl,v'l'}P_l(\theta)P_{l'}(\theta)\delta_T(f_{vl,v'l'}-f)\right|^2, \tag{31}$$

respectively.

2.3.3. Propagation in a continuum-wave laser field. When the molecular ion is exposed to a cw laser field, the expansion (25) of the wave function in terms of the stationary vibrational and rotational eigenfunction is no longer appropriate, since the Hamiltonian now depends on time and molecular orientation. Owing to the time periodicity of the Hamiltonian, however, we can apply Floquet theory [35] to expand the molecular wave function $\psi(\vec{R},\vec{r},t)$ in (5) in terms of laser-electric-field-dressed adiabatic (Floquet) states $\{u_{i,\kappa}\}$ that diagonalize the interaction of the molecular ion with the laser electric field. The evolution of nuclear wave functions $\{\hat{\Xi}_i\}$ on individual time-independent laser-dressed (Floquet) potential surfaces can then be written as

$$\hat{\Xi}_i(R,\theta,t)=\sum_{\kappa} a_{i,\kappa}\,\mathrm{e}^{-\mathrm{i}E_{i,\kappa}t}u_{i,\kappa}(R,\theta). \tag{32}$$

Note that, similarly to (25), we expand $\hat{\Xi}_i$ in ro-vibrational states $u_{i,\kappa}(R,\theta)$ with energies $E_{i,\kappa}$ on each Floquet potential surface. The label i identifies a given Floquet surface, and the index κ collectively specifies ro-vibrational quantum numbers.

As in sections 2.3.1 and 2.3.2, we remove all time-independent terms from the probability density (17). For the present case, this is achieved by omitting all diagonal terms in κ. Adding the contribution from all adiabatic Floquet surfaces, we obtain

$$c(R,\theta,t)=\sum_{i,\kappa\neq\kappa'} a_{i,\kappa}a^*_{i,\kappa'}u_{i,\kappa}(R,\theta)u^*_{i,\kappa'}(R,\theta)\,\mathrm{e}^{-\mathrm{i}(E_{i,\kappa}-E_{i,\kappa'})t}. \tag{33}$$

Fourier transformation in analogy to (28) results in

$$\tilde{c}(R,\theta,f)=\sum_{i,\kappa\neq\kappa'} a_{i,\kappa}a^*_{i,\kappa'}u_{i,\kappa}(R,\theta)u^*_{i,\kappa'}(R,\theta)\delta_T(f_{i,\kappa,\kappa'}-f), \tag{34}$$

where $f_{i,\kappa,\kappa'}=(E_{i,\kappa}-E_{i,\kappa'})/2\pi$ are the QB frequencies on a given Floquet surface i between ro-vibrational states κ and κ'.

In contrast to the field-free result (29), the non-separable dependence of the Hamiltonian in each Floquet channel on R and θ discourages an expansion in products of vibrational and angular eigenfunction, and thus the simplifying orthogonality relations (26) and (27) are not applicable. In comparison with the field-free power spectra (30) and (31), this will complicate the interpretation of the R- and θ-dependent QB spectra in a cw laser field,

$$A(R, f) = \left| \sum_{i,\kappa\neq\kappa'} a_{i,\kappa} a^*_{i,\kappa'} \delta_T(f_{i,\kappa,\kappa'} - f) \int \mathrm{d}\theta \, \sin(\theta) u_{i,\kappa}(R,\theta) u^*_{i,\kappa'}(R,\theta) \right|^2 \quad (35)$$

and

$$W(\theta, f) = \left| \sum_{i,\kappa\neq\kappa'} a_{i,\kappa} a^*_{i,\kappa'} \delta_T(f_{i,\kappa,\kappa'} - f) \int \mathrm{d}R \, u_{i,\kappa}(R,\theta) u^*_{i,\kappa'}(R,\theta) \right|^2 . \quad (36)$$

2.4. *Initial vibrational and rotational distributions*

We model the initial nuclear wave function of the molecular ion by assuming its separation into a solely R- and a solely θ-dependent factor,

$$\Xi_1(R, \theta, t = 0) = \sum_{\nu} a_{\nu,l=0} \chi_{\nu l}(R) \sum_{l} b_l P_l(\theta). \quad (37)$$

The coefficients $a_{\nu,l=0}$ are obtained as the results of a Franck–Condon (FC) transition from the electronic and vibrational ground state of the non-rotating D_2 molecule to the electric ground state of D_2^+. In practice, we find these coefficients by modeling the ground state D_2 nuclear wave function as a Gaussian centered at the equilibrium distance $R = 1.4$ of D_2, whose width we adjust to the ground-state vibrational energy of the neutral molecule.

We model the initial angular wave function as a Boltzmann distribution at a rotational temperature of 250 K. We use real expansion coefficients that are given by the square roots of Boltzmann factors,

$$b_l = \sqrt{\frac{\mathrm{e}^{-\frac{l(l+1)}{2mR^2kT}}}{\sum_{l'=0,2,4} \mathrm{e}^{-\frac{l'(l'+1)}{2mR^2kT}}}}, \qquad l = 0, 2, 4, \quad (38)$$

and assume D_2 molecules with net nuclear spin $I = 0$, allowing only for even values of l. Since the occupation of rotational states with $l > 4$ is negligible at the considered rotational temperature, we only include the lowest even values for l. The top left graph of figure 1 shows the initial ro-vibrational probability density corresponding to (37).

3. Numerical results

3.1. *Quantum-beat spectra for field-free propagation*

We first discuss the transition spectra of the D_2^+ molecular ion without a laser field. In this case, the nuclear wave function components Ξ_i remain uncoupled. Assuming that nuclear motion is initiated in the lowest electronic state of the molecular ions, we can restrict our discussion to the nuclear wave function component Ξ_1. Figure 1 shows snapshots of the field-free evolution of nuclear probability density.

Figures 2–4 reveal the power spectra $A(R, f)$ and $W(\theta, f)$, together with the corresponding line intensities $\mathscr{A}(f)$ and $\mathscr{W}(f)$. Figures 2(a) and (b) display results for molecular ions that are initially aligned with the laser polarization and do not rotate. All other results in figures 2–4 are calculated for freely rotating molecular ions, starting with the coherent initial state (37).

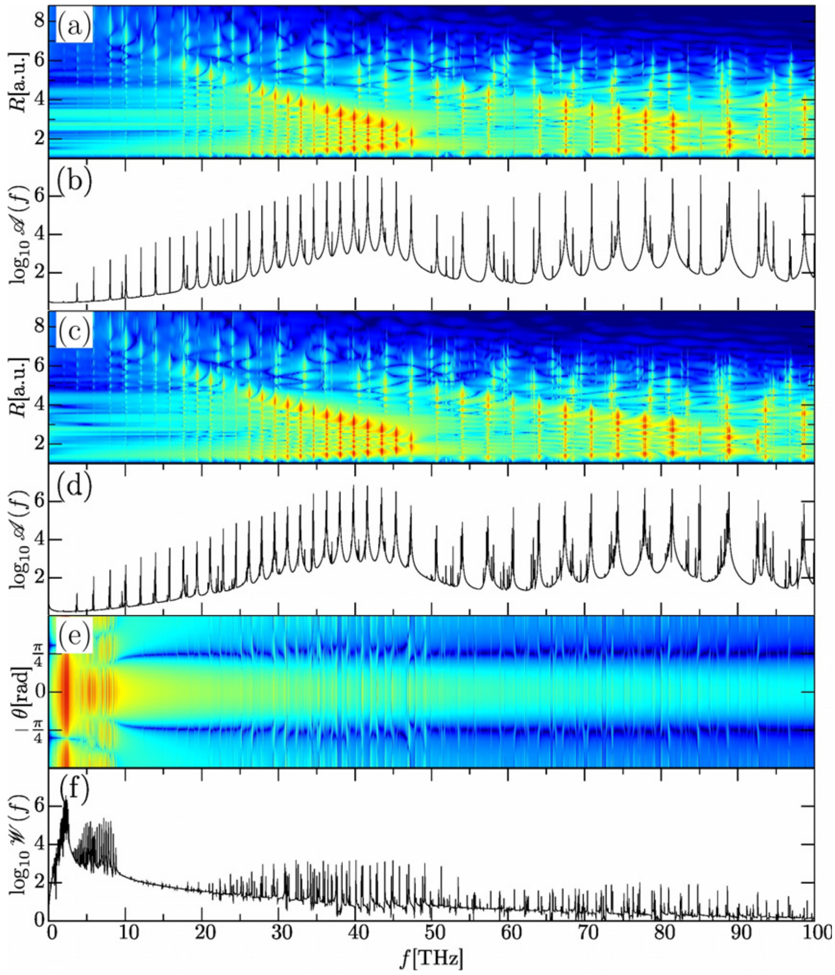

Figure 2. Power spectra $A(R, f)$ (a) and (c), $W(\theta, f)$ (e), and corresponding spectral line intensities $\mathscr{A}(f)$ (b) and (d) and $\mathscr{W}(f)$ (f) for field-free evolution of an aligned (a, b) and rotating (c–f) D_2^+ molecular ion.

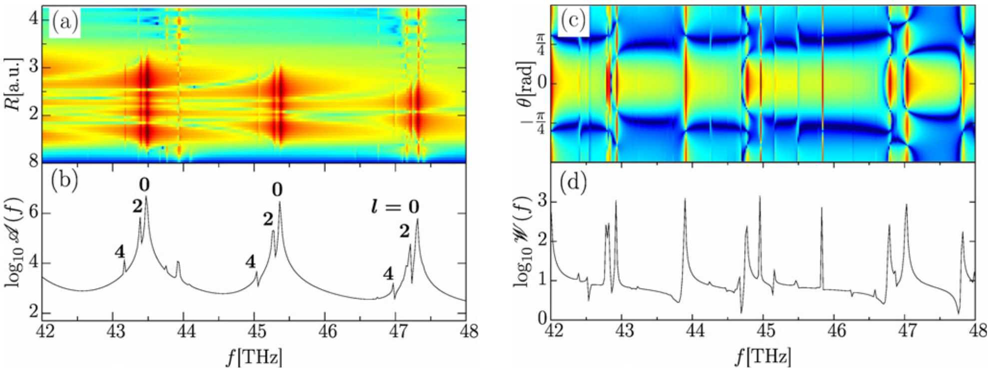

Figure 3. Zoom into specific frequency ranges of figures 2(c)–(f).

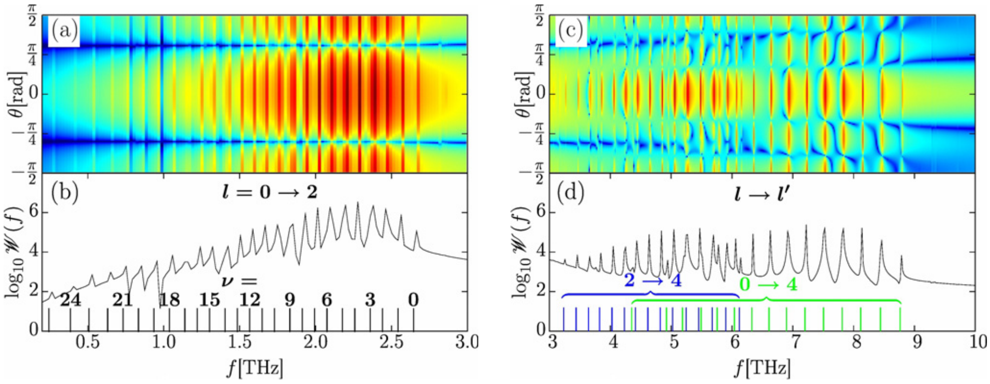

Figure 4. Zoom into specific low-frequency ranges of figures 2(e) and (f). Vibrational quantum numbers are indicated by short vertical lines in (b) and (d).

Figures 2(a)–(d) show QBs between adjacent vibrational states with $\Delta\nu = 1$ below 48 THz, a series of QBs with $\Delta\nu = 2$ below 92 THz, and a weak background of 'intruder' lines corresponding to series of QBs with $\Delta\nu \geqslant 3$. As we can see in figures 2(c) and (d) and 3(a) and (b), every vibrational transition $\nu \to \nu'$ is split into multiple lines that correspond to different rotational states l in (30). These lines display ro-vibrational couplings, because the energies $E_{\nu l}$ of the system cannot be written as a sum of vibrational and rotational energies ($E_{\nu l} \neq E_\nu + E_l$). If the energies $E_{\nu l}$ could be written as a sum of vibrational and rotational energies, these ro-vibrational manifolds would collapse to just one line at the frequency $2\pi f_{\nu l,\nu' l} = E_{\nu l} - E_{\nu' l} = (E_\nu + E_l) - (E_{\nu'} + E_l) = E_\nu - E_{\nu'}$. To understand which vibrational transition belongs to which l, we add the centrifugal kinetic energy $l(l+1)/(2\mu R^2)$ to the ground-state BO surface to obtain the effective potential $V_{\text{eff}}(R) = E_1(R) + l(l+1)/(2\mu R^2)$. In this potential, the distances between consecutive vibrational eigenenergies for larger l are smaller, such that the transition frequencies $f_{\nu l,\nu' l}$ decrease with increasing l. Therefore, vibrational transitions for larger l can be found at lower frequencies. The spacing between two neighboring rotational lines increases with increasing l, since $l(l+1)/(2\mu R^2)$ depends quadratically on l.

To support the statements of the previous paragraph, figures 3(a) and (b) take a closer look at the three vibrational transitions ($0 \to 1$, $1 \to 2$ and $2 \to 3$) in the frequency interval between 42 and 48 THz. The plots show that each vibrational transition appears three times. This results from the construction of the initial wave function (37), where only small $l (= 0, 2, 4)$ are included. If more rotational states were initially populated, one would observe a larger number of lines in these spectra. Note that the distance between two neighboring lines increases with l.

Before discussing the θ-dependent power spectra, we examine the overlap matrix

$$S_{\nu l,\nu' l'} = \int_0^\infty \mathrm{d}R\, \chi_{\nu l}(R) \chi^*_{\nu' l'}(R) \tag{39}$$

defined in (27). The stationary vibrational states are obtained by solving the Schrödinger equation

$$\left(\frac{\mathrm{d}^2}{\mathrm{d}R^2} + E_1(R) + \frac{l(l+1)}{2\mu R^2} \right) \chi_{\nu l}(R) = E_{\nu l} \chi_{\nu l}(R). \tag{40}$$

For small values of $\Delta l = l - l'$ (which is the case for our initial wave function), the overlap $S_{\nu l,\nu l'}$ with $l \neq l'$ of two vibrational states will be close to one, since their effective potentials

$E_1(R)+\frac{l(l+1)}{2\mu R^2}$ do not differ by much. For the same reason, the overlap $S_{\nu l,\nu' l'}$ with $\nu \neq \nu'$ and $l \neq l'$ will be close to zero.

The θ-dependent spectra (31) consist of two parts. The first part (first line in (31)) describes the pure rotational beats, whereas the second part (second line in (31)) describes ro-vibrational beats. The first part is dominant, because the second contains overlap integrals of different vibrational states that are close to zero. By looking at the spectral line intensity $\mathscr{W}(f)$ (figure 2(f)), we can clearly identify these two parts: in the dominant frequency range ($f < 10$ THz), the intensity is two orders of magnitude higher than for the remainder of the spectrum ($f > 10$ THz).

After these preliminary remarks, we can analyze the dominant part of the θ-dependent spectra, starting with figure 4, which maps $l \to l'$ rotational transitions in $W(\theta, f)$ and $\mathscr{W}(f)$. As shown in (31), there is a series of rotational transitions with a different nodal structure for every vibrational state ν. The transition frequencies $f_{\nu l,\nu l'}$ for a fixed Δl $(= l - l')$ decrease for increasing ν. This can be understood by means of some basic considerations. For a given angular momentum and mass, the rotational energy $l(l+1)/(2\mu R^2)$ of a rigid rotor decreases with R^{-2}. Thus, the expectation value of R^{-2} in the electronic ground state decreases for increasing vibrational excitation ν. This means that the ro-vibrational transition frequency for a higher vibrational state is lower than for a lower vibrational state. Note that all these lines would coincide if there were no ro-vibrational coupling.

Figures 4(a) and (b) zoom in on the ro-vibrational QB lines of figures 2(e) and (f) in the energy interval between 0.2 and 3 THz for $l = 0 \to 2$ transitions. We recall that the initial D_2^+ wave function was assumed to be the result of an FC transition from D_2, yielding a relatively broad vibrational states distribution. We also recall that the molecular ion is assumed to be rather cold rotationally. Due to this particular choice of the initial nuclear wave packet in the present study, there are many more ‘vibrational satellite’ lines for a given Δl than there are ‘rotational satellite’ lines for any given $\Delta\nu$. This is clearly seen by comparing figures 3(a) and 4(a). The ordering of the $l = 0 \to 2$ QB lines in figure 4(a) is such that the vibrational satellite lines for the vibrational ground state ($\nu = 0$) have the highest frequency. Vibrational satellites for increasing $\nu \geqslant 1$ appear at successively smaller frequencies.

In order to (i) better understand the ro-vibrational spectra in figures 2–4 and (ii) clearly resolve angular nodes of the stationary rotational states, we show in figures 5(a)–(c) the results obtained in fixed-rotor approximation. In this approximation, the expectation value of R^{-2} is calculated for a given vibrational state ν and subsequently used in the kinetic energy of the rigid rotor, $l(l+1)/(2\mu)\langle R^{-2}\rangle$. For figures 5(a), (b), and (c), we chose the vibrational ground state ($\nu = 0$, with $\langle R^{-2}\rangle = 0.2455$), the 8th excited state ($\nu = 8$, with $\langle R^{-2}\rangle = 0.1774$), and the 16th excited state ($\nu = 16$, with $\langle R^{-2}\rangle = 0.1138$), respectively. The different rotational energies result in noticeably different rotational transition lines. The lowest spectral line in figures 5(a)–(c) can only correspond to the rotational QBs of the $l = 0$ and $l = 2$ rotational states, because the nodal structure of this line does not fit any other rotational transition (the Legendre polynomial P_0 has no nodes and P_2 has two). The next higher spectral line corresponds to QBs of $l = 2$ with $l = 4$. This spectral line has six nodes. Here, transitions from $l = 0$ to $l = 6$ would generate the same number of nodes, but the $l = 6$ state is not included in the initial wave function. The third spectral line, which is distinctly visible in these three spectra, corresponds to the interference of $l = 0$ and $l = 4$ stationary rotational states. The displayed nodal structure fits only this transition, and the energy difference is larger than for the previously discussed two lines. It is noteworthy that the $l = 2 \to 4$ line in figure 5(b) has a higher energy than the $l = 0 \to 4$ transition in figure 5(c).

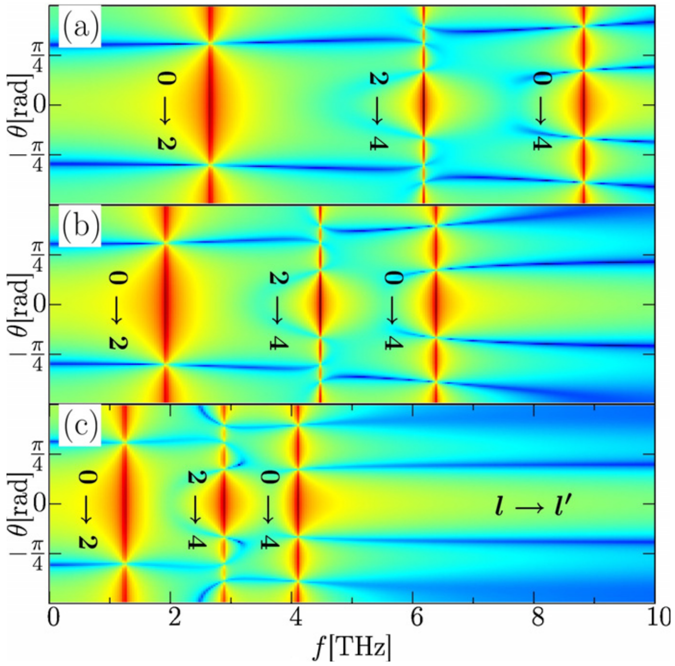

Figure 5. Power spectrum $W(\theta, f)$ for the field-free evolution of an initial rotational nuclear wave packet in fixed-rotor approximation. The internuclear distance is chosen as the expectation value of R^{-2} in the vibrational ground state (a), for the $\nu = 8$ excited vibrational state (b), and for the $\nu = 16$ excited vibrational state (c) of the $1\,\mathrm{s}\sigma_\mathrm{g}$ potential surface.

Accordingly, series of rotational QB frequencies for different Δl overlap. This is clearly seen in, and complicates, the interpretation of figure 4(c).

3.2. *Quantum-beat spectra for realistic probe pulses*

In this section, we discuss our numerical results for the evolution of a ro-vibrational wave packet under the influence of a $\sin^2$ 50 fs (full-width at half-maximum (FWHM)) $10^{14}\,\mathrm{W\,cm^{-2}}$ probe pulse pedestal. The interaction of the pedestal with the probe laser pulse significantly modifies the nuclear dynamics in the molecular ion immediately before its destructive imaging by the short and intense main part of the probe pulse. Note that we do not propagate the nuclear wave function through the entire probe pulse, but instead terminate the propagation at the center of the pedestal without including the main probe pulse. In this way, we simulate the evolution of the nuclear wave function up to the point in time at which it would be probed (i.e. Coulomb-explosion imaged) by an ideal ultrashort probe pulse that instantaneously ionizes the molecular ion without any prior distortion [22]. The interaction with the probe pulse pedestal enables electronic excitations of the molecular ion, which we allow for by including the first- and second-excited BO state σ_u and π_u in (5), in addition to the electronic ground state ($1\mathrm{s}\sigma_\mathrm{g}$). We compare these results with previous rotation-free calculations [21].

Figure 6(a) shows the R-dependent power spectrum. The corresponding line intensity is shown in figure 6(b). In the frequency interval between 40 and 50 THz, the nodal structure is

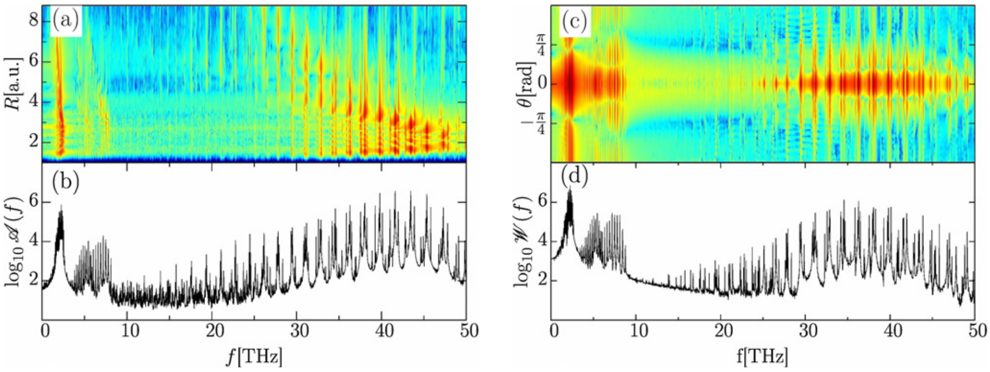

Figure 6. Power spectra $A(R, f)$ (a) and $W(\theta, f)$ (c) and the corresponding spectral line intensities $\mathscr{A}(f)$ (b) and $\mathscr{W}(f)$ (d), including a $10^{14}\,\mathrm{W\,cm^{-2}}$ probe pulse pedestal (see text).

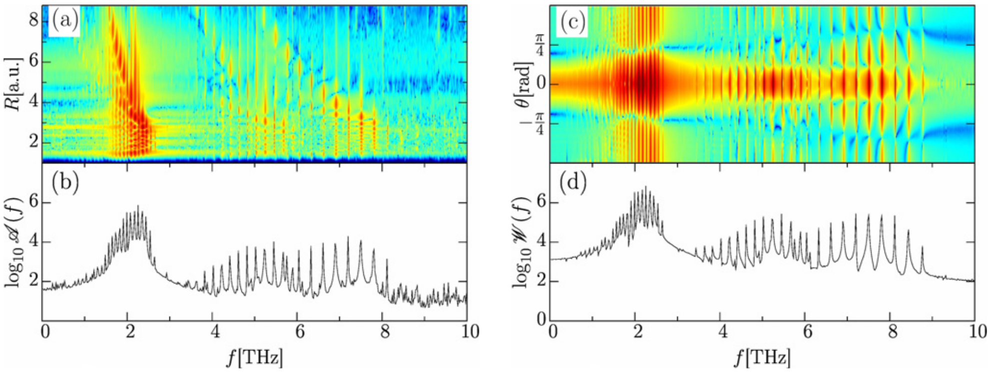

Figure 7. Zoom into the low-frequency range of figure 6.

identical to the one shown for laser-free propagation in the previous section. The most striking changes induced by the probe pulse pedestal appear at frequencies below 40 THz. Between 25 and 30 THz, 1ω bond softening [22] allows the molecular ion to dissociate over the barrier in the lowest laser-induced (Floquet) potential surface after the net absorption of one photon. In this calculation, we do not find evidence for 1ω bond hardening [22], i.e., the transient trapping of nuclear probability density in a laser-electric-field-dressed adiabatic potential surface due to the absorption of one photon. At the considered high pedestal intensity, evidence for bond-softening dissociation via the 3ω resonance is visible near 40 THz in figure 6(a).

Bond softening and evidence for bond hardening were discussed for non-rotating molecules in the literature (see [21, 22] and references therein). New effects that are induced by the rotation of the molecule appear below 10 THz, where a large number of spectral lines emerge. These were found neither in rotation-free calculations [21] nor in our field-free calculations including rotation (figures 2(c) and (d)). To explain these new lines, figure 7 zooms into the low-frequency range of figure 6. Figures 7(c) and (d) show, at high resolution, the main rotational QBs in $W(\theta, f)$ and $\mathscr{W}(f)$, which are also visible in figures 6(c) and (d). In figures 7(a) and (b), the same frequency range is mapped for $A(R, f)$ and $\mathscr{A}(f)$. When we compare figures 7(b) and (d), we find a match in the frequencies of these new lines and the main rotational QBs ($l = 0 \rightarrow 2$, $2 \rightarrow 4$ and $0 \rightarrow 4$). These additional lines in figure 6(a) result from

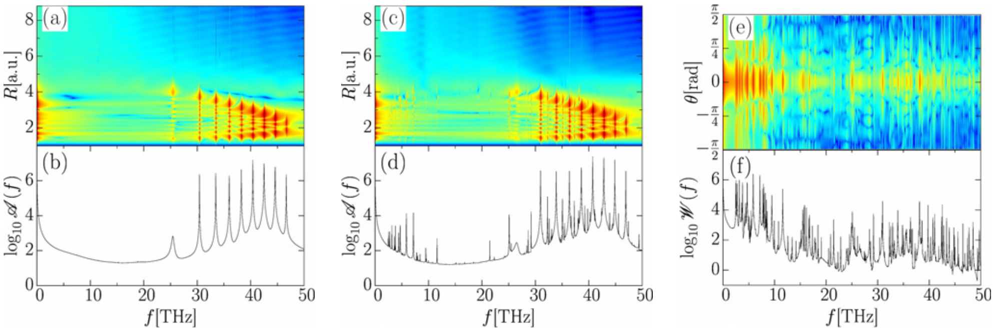

Figure 8. Graphs (a)–(f) are the same as in figure 2, but for the evolution of D_2^+ ro-vibrational nuclear wave packets in a $10^{13}\,\mathrm{W\,cm^{-2}}$ cw laser.

the fact that the orthogonality relations (26) and (27) used in the field-free case are weakened, such that rotational QBs appear in the R-dependent spectra. Similarly, vibrational QBs can now be found in the θ-dependent spectra.

3.3. *Quantum-beat spectra in a continuum-wave field*

Next, we discuss the ro-vibrational QB spectra of D_2^+ in a cw laser field. We assume a turn-on time of 10 optical cycles ($\approx$27 fs) for a cw laser field with a $\sin^2$ ramp starting at $t = 0$ and the same initial wave function (37) as in sections 3.1 and 3.2.

Figures 8(c)–(f) show the spectra of a rotating molecule, whereas figures 8(a) and (b) show $A(R, f)$ and $\mathscr{A}(f)$ for the special case where the molecular axis remains aligned with the laser. In figure 8(c), vibrational transitions are mapped and their nodal structure is clearly reproduced. In comparison with figure 8(a), we notice that there are no QBs below 25 THz. In contrast, figure 8(d) shows spectral lines below 12 THz.

The intensity distribution of ro-vibrational lines is distinctly different for the R- and θ-dependent power spectra, due to different vibrational and rotational level spacings. In figure 8(d), the strongest lines occur at frequencies above 30 THz, and correspond to QBs between the initially populated vibrational states. All other lines are comparatively weak. In contrast, figure 8(f) is dominated by strong lines below 12 THz, while all lines at higher frequencies are weak in comparison.

A closer look at figures 8(d) and 8(f) reveals that the beat frequencies in both spectra are equal. To understand this, we revisit the derivation of the power spectra in section 2.3.3. Orthogonality relations (26) and (27) do not hold for the interaction with a cw laser, such that the nuclear wave functions are not separable into angular and radial factors. Therefore, for the propagation in a cw laser electric field, the two integrations needed to arrive at $A(R, f)$ and $W(\theta, f)$ merely cause different line strengths. In contrast to laser-free propagation, where the integrations over θ and R in (30) and (31) eliminate a large number of ro-vibrational transition frequencies by virtue of the orthogonality of stationary vibrational and rotational nuclear wave functions, no such reduction in the number of QB lines occurs for the interaction with a cw laser. This complicates the identification of rotational and vibrational QBs in the power spectra and the assignment of vibrational (rotational) satellites to a given rotational (vibrational) state. This is also expressed by the fact that the index κ in (32) refers to both rotational and vibrational states, such that rotational and vibrational beats now emerge simultaneously. Physically this is

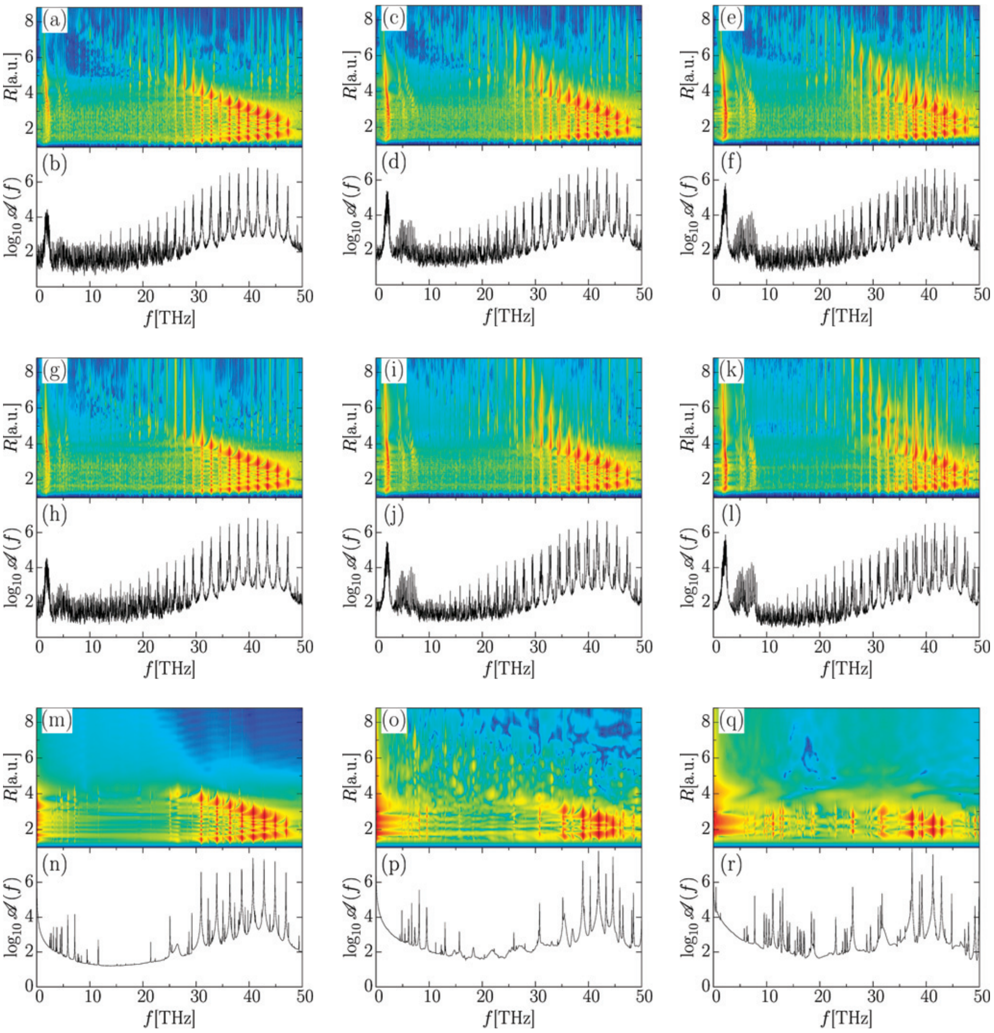

Figure 9. QB spectra $A(R, f)$ and $\mathscr{A}(f)$ for different intensities and pulse lengths: the intensities are $10^{13}\,\mathrm{W\,cm^{-2}}$ on the left, $5\times10^{13}\,\mathrm{W\,cm^{-2}}$ in the middle and $10^{14}\,\mathrm{W\,cm^{-2}}$ on the right. The probe pulse pedestal is 25 fs long (FWHM) in the two top rows (graphs (a)–(f)) and 50 fs (FWHM) in the two middle rows (graphs (g)–(l)). The two bottom rows (graphs (m)–(r)) show results for a cw laser.

due to the sustained non-separability of the molecular ions' vibrational and rotational motion in a cw laser field.

3.4. Laser intensity and pulse length dependence

In this section, we investigate the dependence of R-dependent QB spectra of ro-vibrating molecular ions on the intensity and duration of the probe pulse pedestal. By doubling the probe pulse pedestal duration of the $\sin^2$ pulse from 25 fs (FWHM) (two top rows in figure 9, graphs (a)–(f)) to 50 fs (two middle rows in figure 9, graphs (g)–(l)), the spectral density at higher values of R increases. This is consistent with a longer pulse being able to transfer more energy to the molecular ions, which, in addition, have more time to dissociate by bond softening. For the cw laser (two bottom rows in figure 9, graphs (m)–(r)), all higher vibrational states are fully depleted by bond softening. Their probability density is far outside the displayed R range, such that the bond-softening process is less obviously imaged than for the pulsed laser interactions. Due to the long exposure to the cw laser electric field, all vibrational QB lines are ac-Stark shifted to lower frequencies.

In section 3.2, we found that the laser weakens orthogonality relations (26) and (27). At higher intensities, we find that the same effect is enhanced. The line intensity of the spectral lines below 10 THz grows for increasing laser intensity. For an intensity of $10^{14}\,\mathrm{W\,cm^{-2}}$ (figures 9(e) and (k)), 3ω bond softening near 40 THz is visible.

4. Conclusions

We applied internuclear distance and molecular orientation-dependent Fourier transformation imaging in order to analyze ro-vibrational nuclear motion in coherently ro-vibrationally excited D_2^+. We discussed how this imaging method can be used to display (i) the nodal structure of the bound vibrational and rotational wave function, (ii) the laser-electric-field-dressed adiabatic molecular potential surfaces, (iii) the ro-vibrational transition energies and (iv) the emergence of vibrational and rotational QB multiplets. These multiplets are due to the coupling of rotational and vibrational degrees of freedom. Examination of their line strengths allows the quantitative assessment of ro-vibrational couplings. For the future, QB spectroscopy offers the prospect of imaging laser-dressed molecular potential surfaces of (small) molecules, based on a time series of measured angle-resolved KER spectra.

Acknowledgments

We thank Burkhard Schmidt for his advice in the implementation of the computer code *wave packet*. This work was supported by the NSF and the Division of Chemical Sciences, Office of Basic Energy Sciences, Office of Energy Research, US DOE.

Appendix A. Numerical propagation of the nuclear wave function

In order to propagate the nuclear wave function $\vec{\Xi}(R,\theta,t)$ on a two-dimensional numerical grid, we use the split-time-evolution operator in equation (16) and successively apply, from right to left, each exponential operator to the wave function components $\{\Xi_i\}$. In position representation, the first, second, fourth and fifth exponents are complex-valued functions, while the kinetic energy term (12) is a differential operator.

In order to take advance of the diagonal representation of the kinetic energy operator in momentum space, we fast Fourier transform [36] the wave function before applying the kinetic energy term in (12),

$$\tilde{\Xi}_i(P,\theta,t) = \frac{1}{\sqrt{2\pi}} \int_0^\infty \mathrm{d}R\ \Xi_i(R,\theta,t)\mathrm{e}^{-\mathrm{i}PR}. \tag{A.1}$$

We truncate the integral over R and choose an equidistant R grid with M points in the interval $[R_{\min}, R_{\max}]$. We approximate the infinitesimal line element $\mathrm{d}R$ by the finite difference

$\Delta R = (R_{\max} - R_{\min})/M$, represent the wave function at the grid points $R_k = R_{\min} + k\Delta R$ with $k = 0, 1, \ldots, M-1$, and obtain

$$\tilde{\Xi}_i(P_j, \theta, t) \approx \frac{1}{\sqrt{2\pi}} \sum_{k=0}^{M-1} \Delta R\ \Xi_i(R_k, \theta, t)\mathrm{e}^{-\mathrm{i}P_j R_k}. \tag{A.2}$$

With regard to θ dependence, we expand in Legendre polynomials P_l, taking advantage of the conserved nuclear angular momentum component along the laser polarization (z-direction). Introducing $x = \cos\theta$, we numerically calculate the angular momentum projections

$$\Xi_{i,l}(R, t) = \int_{-1}^{1} \mathrm{d}x\ P_l(x)\Xi_i(R, \theta, t) \tag{A.3}$$

by Gaussian quadrature, evaluating the integrand at non-equidistant points x_n with different weights w_n at each point (for a detailed explanation, see [37]),

$$\Xi_{i,l}(R, t) \approx \sum_{n=0}^{N-1} w_n P_l(x_n)\Xi_i(R, x_n, t). \tag{A.4}$$

The Gaussian quadrature (A.4) provides the exact result (A.3) if the integrand is a polynomial of degree $(2N-1)$ or less. Otherwise, its error

$$\int_{-1}^{1} f(x)\mathrm{d}x - \sum_{n=0}^{N-1} w_n f(x_n) = \frac{2^{2N+1}(N!)^4}{(2N+1)[(2N)!]^3} f^{(2N)}(\xi), \quad (-1 < \xi < 1) \tag{A.5}$$

is proportional to the $(2N)$th derivative of the integrand. In our case ($m = 0$), the quadrature points are the N zeros of the Legendre polynomial $P_N(x)$, and the w_n are the corresponding weights.

Appendix B. Numerical values

In this section, we list the numerical parameters used. For the discrete Fourier transformation (A.2), the finite integration interval $[R_{\min}, R_{\max}]$ is [0.2, 15]. In order to use the fast Fourier transformation algorithm, we split the integration interval into $256 = 2^8$ parts. For the $x = \cos\theta$ integration, we used 30 grid points. We perform the time propagation using equidistant time steps $\Delta t = 0.01$ over a sampling time of $T = 49$ ps.

References

[1] Gruebele M and Zewail A H 1993 *J. Chem. Phys.* **98** 883

[2] Zewail A H 2000 *J. Chem. Phys.* A **104** 5660

[3] Brixner T, Pfeifer T, Gerber G, Wollenhaupt M and Baumert T 2005 *Femtosecond Laser Spectroscopy* ed P Hannaford (Berlin: Springer) chapter 9

[4] Alnaser A S *et al* 2005 *Phys. Rev.* A **72** 030702

[5] Légaré F, Lee K F, Litvinyuk I V, Dooley P W, Bandrauk A D, Villeneuve D M and Corkum P B 2005 *Phys. Rev.* A **72** 052717

[6] Ergler Th, Rudenko A, Feuerstein B, Zrost K, Schröter C D, Moshammer R and Ullrich J 2006 *Phys. Rev. Lett.* **95** 193001

[7] Baker S, Robinson J S, Haworth C A, Teng H, Smith R A, Chirila C C, Lein M, Tisch J W G and Marangos J P 2006 *Science* **312** 424

[8] Hertel I V and Radloff W 2006 *Rep. Prog. Phys.* **69** 1897

[9] Staudte A *et al* 2007 *Phys. Rev. Lett.* **98** 073003

[10] Feuerstein B, Ergler Th, Rudenko A, Zrost K, Schröter C D, Moshammer R, Ullrich J, Niederhausen T and Thumm U 2007 *Phys. Rev. Lett.* **99** 153002

[11] He F, Becker A and Thumm U 2008 *Phys. Rev. Lett.* **101** 213002

[12] Murphy D S, McKenna J, Calvert C R, Bryan W A, English E M L, Wood J, Turcu I C E, Newell W R, Williams I D and McCann J F 2007 *J. Phys. B: At. Mol. Opt. Phys.* **40** S359

[13] Sandhu A S, Gagnon E, Santra R, Sharma V, Li W, Ho P, Ranitovic P, Cocke C L, Murnane M M and Kapteyn H 2008 *Science* **322** 1081

[14] Krausz F and Ivanov M 2009 *Rev. Mod. Phys.* **81** 163

[15] Feuerstein B and Thumm U 2003 *Phys. Rev.* A **67** 063408

[16] Chelkowski S, Bandrauk A D, Staudte A and Corkum P B 2007 *Phys. Rev.* A **76** 013405

[17] Rudenko A *et al* 2006 *Chem. Phys.* **329** 193

[18] Niikura H, Villeneuve D M and Corkum P B 2006 *Phys. Rev. Lett.* **73** 021402

[19] Martín F *et al* 2007 *Science* **315** 629

[20] Bocharova I A, Mashiko H, Magrakvelidze M, Ray D, Ranitovic P, Cocke C L and Litvinyuk I V 2008 *Phys. Rev.* A **77** 053407

[21] Thumm U, Niederhausen T and Feuerstein B 2008 *Phys. Rev.* A **77** 063401

[22] Makrakvelidze M, He F, Niederhausen T, Litvinyuk I V and Thumm U 2009 *Phys. Rev.* A **79** 033410

[23] Lagmago G, Kamta and Bandrauk A D 2005 *Phys. Rev. Lett.* **94** 203003

[24] Tong X M and Lin C D 2007 *Phys. Rev. Lett.* **98** 123002

[25] Pieper S and Lein M 2008 *Phys. Rev.* A **77** 041403

[26] Anis F and Esry B 2008 *Phys. Rev.* A **77** 033416

[27] Winter M, Schmidt R and Thumm U 2009 *Phys. Rev.* A **80** 031401

[28] Feuerstein B and Thumm U 2003 *Phys. Rev.* A **67** 043405

[29] Niederhausen T and Thumm U 2008 *Phys. Rev.* A **77** 013407

[30] Kunert T and Schmidt R 2003 *Eur. Phys. J.* D **25** 15 and www.dymol.org

[31] Extensible computational chemistry environment basis set database, version 02.02.06 http://www.emsl.pnl.gov/forms/basisform.html

[32] Wind H 1965 *J. Chem. Phys.* **42** 2371

[33] Feit M D, Fleck J A Jr and Steiger A 1982 *J. Comput. Phys.* **47** 412

[34] www.wavepacket.sourceforge.net

[35] Sambe H 1973 *Phys. Rev.* A **7** 2203

[36] Frigo M and Johnson S G 2005 The Design and Implementation of FFTW3 *Proc. IEEE* **93** 216–31

[37] Tannor D J 2006 *Introduction to Quantum Mechanics: a Time-Dependent Perspective* (Sausalito, CA: University Science Books)